Unified Solution of Conjugate Fluid and Solid Heat Transfer – Part I. Solid Heat Conduction

Shu-Jie Li^{1,*}and Lili Ju²

Abstract. A unified solution framework is proposed for efficiently solving conjugate fluid and solid heat transfer problems. The unified solution is solely governed by the compressible Navier-Stokes (N-S) equations in both fluid and solid domains. Such method not only provides the computational capability for solid heat transfer simulations with existing successful N-S flow solvers, but also can relax time-stepping restrictions often imposed by the interface conditions for conjugate fluid and solid heat transfer. This paper serves as Part I of the proposed unified solution framework and addresses the handling of solid heat conduction with the nondimensional N-S equations. Specially, a parallel, adaptive high-order discontinuous Galerkin unified solver has been developed and applied to solve solid heat transfer problems under various boundary conditions.

AMS subject classifications: 65M22, 76N06

Key words: Conjugate heat transfer, solid heat conduction, compressible Navier-Stokes, exponential time integration

1 Introduction

Conjugate fluid and solid heat transfer problems exist in many areas of science and engineering, such as turbomachinery, heat exchangers, and semiconductor devices. A conventional way of solving the conjugate heat transfer problem is to combine the Navier-Stokes (N-S) equations for the fluid with the Fourier-Biot (F-B) equation for the solid [6, 19], and two stand-alone solvers representing each physic are loosely coupled by exchanging physical parameters through the domain interface conditions [22,24–26]. However, coupling in this way often leads to stability constraints and very restrictive time steps [4, 20], which makes the approach less efficient. The other approach is to develop a fully coupled discretization method modeling both the solid

Email: shujie@csrc.ac.cn (Shu-Jie Li), ju@math.sc.edu (Lili Ju)

¹ Division of Mechanics, Beijing Computational Science Research Center, Beijing 100193, China

² Department of Mathematics, University of South Carolina, Columbia, SC 29208, USA

^{*}Corresponding author.

and the fluid with appropriate interface conditions. However, the production of a single code with the strong coupling of the N-S and the F-B equations can be as much work as writing individual codes for separate fluid and solid applications, and is hard to utilize advanced numerical capabilities of the existing fluid and solid solvers [8,17].

For conjugate heat transfer with incompressible flows, the solid heat transfer phenomena can be modeled either by the F-B equation or using the incompressible N-S equations also in the solid domain. The latter strategy is possible since the energy equation in the incompressible N-S equations decouples from the continuity and momentum equations. However, the situation is essentially different for the compressible N-S equations where the energy equation does not decouple from the continuity and momentum equations. In [18], Nordström et al. present the similarity condition for the compressible N-S equations and the F-B equation. In their work, the velocities are uncoupled and the fluid and the solid domains are explicitly coupled by continuity of temperature and heat fluxes, but this approach still suffers from stability issues. The goal of this work is to develop a unified solution solver which can fully inherit the advanced computational capabilities of the existing N-S flow solver, resulting in an all-variable coupled method to efficiently simulate conjugate fluid and solid heat transfer problems. In the proposed method, the unified solution in both the fluid and solid domains is solely governed by the full compressible N-S equations in a nondimensional form. It belongs to the fully coupled discretization of fluid and solid which can thus relax the time step restriction existing in the loose coupling methods. Additionally, a new capable solid solver equipped with state-of-the-art computational fluid dynamics (CFD) methods can be obtained with the proposed unified solution strategy.

This paper serves as Part I of the proposed unified solution framework and focuses on applying the compressible N-S equations to model and solve the solid heat transfer problems. Various advanced CFD methods with fast exponential integrator-based time marching [9–16] can be utilized to compute the solid solutions and provide more computational capabilities than traditional solid heat transfer solvers. The capabilities of using an adaptive high-order discontinuous Galerkin (DG) N-S solver for various solid heat transfer problems will be tested with convection and radiation effects.

The remaining parts of this paper are organized as follows. Section 2 presents the theory and equations of the unified solution for solid heat conduction, and Section 3 introduces the numerical methods used in the existing N-S flow solver. Several solid heat transfer problems are tested in Section 4 to demonstrate the capability of the proposed method. Some concluding remarks are finally given in Section 5.

2 Governing Equations

The full, compressible N-S equations govern the transport processes of mass, momentum, and energy, where the energy equation is proved mathematically connected to the F-B equation [18]. We will show in this section that by using proper nondimensionalization, initial and boundary conditions, the F-B equation is also physically con-

sistent with the energy equation of the N-S equations.

2.1 The compressible Navier-Stokes equations

In the proposed unified solution of conjugate fluid and solid heat transfer, the problem is solely governed by the conservative form of the compressible N-S equations with a source term as follows:

$$\mathbf{U}_t + \nabla \cdot \mathbf{F}_c = \nabla \cdot \mathbf{F}_v + \mathbf{S} \tag{2.1}$$

where the conservative vector \mathbf{U} , the convection flux \mathbf{F}_c , the viscous flux \mathbf{F}_v and the source term \mathbf{S} are respectively written as

$$\mathbf{U} = \begin{bmatrix} \rho \\ \rho \mathbf{v} \\ \rho E \end{bmatrix}, \quad \mathbf{F}_c = \begin{bmatrix} \rho \mathbf{v} \\ \rho \mathbf{v} \otimes \mathbf{v} + \rho \mathbf{I} \\ \rho \mathbf{v} H \end{bmatrix}, \quad \mathbf{F}_v = \begin{bmatrix} 0 \\ \tau \\ \tau \cdot \mathbf{v} - \mathbf{q} \end{bmatrix}, \quad \mathbf{S} = \begin{bmatrix} 0 \\ \mathbf{0} \\ Q \end{bmatrix}.$$
(2.2)

Here ρ is the fluid density, \mathbf{v} the fluid velocity, E the total energy, E the total energy, E the fluid heat flux vector, and E0 the volume heat source. The viscous stress E1 is given by

$$\boldsymbol{\tau} = \mu \left[-\frac{2}{3} (\nabla \cdot \mathbf{v}) \mathbf{I} + \nabla \mathbf{v} + (\nabla \mathbf{v})^T \right]$$
 (2.3)

with I denoting the identity tensor. The heat flux is given by

$$\mathbf{q} = -k \, \nabla T, \tag{2.4}$$

where *T* is the temperature and *k* is the thermal conductivity. Additionally, the equation of state of perfect gas is used to close the system, namely,

$$p = \rho RT, \tag{2.5}$$

where $R = C_p - C_v$ is the specific gas constant with C_p and C_v being the specific heat capacity for constant pressure and volume respectively.

2.2 Transformation from the N-S equations to the F-B equation

In the compressible N-S equations (2.2), the first two equations govern the transport processes of mass, momentum, and the last energy equation is similar to the F-B equation which governs the solid heat transfer phenomena. Nordström et al. [18] proved that the F-B equation and the energy component in the Navier-Stokes equations produces exactly the same results only if a similarity condition is hold. Alternately, physical transformations are also possible to transform the energy equation to the F-B equation. Considering rigid solid body with zero velocity in the Eulerian reference frame-

work, (2.2) becomes

$$\mathbf{U} = \begin{bmatrix} \rho \\ \rho \mathbf{v} \\ \rho E \end{bmatrix}, \quad \mathbf{F}_c = \begin{bmatrix} 0 \\ p \mathbf{I} \\ 0 \end{bmatrix}, \quad \mathbf{F}_v = \begin{bmatrix} 0 \\ \mathbf{0} \\ -\mathbf{q} \end{bmatrix}, \quad \mathbf{S} = \begin{bmatrix} 0 \\ \mathbf{0} \\ Q \end{bmatrix}. \tag{2.6}$$

To fully recover the F-S equation, the fluid density ρ and thermal conductivity k can be redefined respectively as

$$\rho := \rho_s \frac{C_s}{C_v}, \quad k := k_s, \tag{2.7}$$

where the subscript s is used to denote the variables and parameters of solid domain problem. Specifically, C_s is the solid specific heat capacity, ρ_s the solid mass density and k_s the solid thermal conductivity. The solid mass density ρ_s is constant in time but can be spatially varying according to the mass conservation equation of (2.1). By substituting (2.7) into (2.1), the energy equation can be transformed to the F-B equation of the form:

$$\frac{\partial \left(\rho_s C_s T\right)}{\partial t} = k_s \nabla^2 T + Q. \tag{2.8}$$

This derivation confirms the similarity condition [18] of the compressible N-S equations and the F-S equation in physics. It can be easily verified that the parametric relationship (2.7) that substitutes the fluid variables with the solid ones also satisfies the similarity condition exactly. As a consequence, in theory, one can obtain the solid solutions by solving the compressible N-S equations despite that there are still some unsolved problems such as non-zero velocity and stability issues [18].

2.3 Solid heat conduction solutions of the nondimensional N-S equations

Nondimensionalizing the flow-field parameters can remove the necessity of converting from one unit system to another within the unified solver and facilitate multiphysics computations with input nondimensional numbers. For the 3-D compressible N-S equations (2.1) for conjugate heat transfer, parameters from both the fluid and the solid domains will be chosen for obtaining a unified solution form. For solid heat transfer problems, the nondimensionalization is performed as follows

$$\rho = \frac{\hat{\rho}}{\rho_{\text{eff}}}, \quad \mathbf{v} = \frac{\hat{\mathbf{v}}}{a_0}, \quad \mathbf{x} = \frac{\hat{\mathbf{x}}}{L_r}, \quad L_r = \frac{\hat{L}}{L_m}, \quad T = \frac{\hat{T}}{T_0},
t = \frac{\alpha_0 \hat{t}}{L_r^2}, \quad p = \frac{\hat{p}}{\rho a_0^2}, \quad E = \frac{\hat{E}}{a_0^2}, \quad k_s = \frac{\hat{k}}{k_0}, \quad \mu = \frac{\hat{\mu}}{\mu_0}.$$
(2.9)

The superscript $\hat{}$ indicates the dimensional quantity. The effective fluid density $\rho_{\rm eff} = \rho_{\rm s}C_{\rm s}/C_{\rm v}$ is used according to (2.7); The dimensional reference states T_0 and a_0 denote the fluid reference temperature and sound speed respectively; k_0 is the solid thermal

conductivity at the reference temperature T_0 , $\alpha_0 = k_s^0/(\rho_s C_s)$ is the solid thermal diffusivity , \hat{L} is the characteristic length of the physical problem, and L_m corresponds to the nondimensional characteristic length of the generated mesh, and μ_0 is the fluid viscosity at T_0 . With the above nondimensionalization process (2.9), the equation of state (2.5) is transformed to

$$p = \frac{\rho T}{\gamma},\tag{2.10}$$

where the ratio of specific heats γ is defined as $\gamma = C_p/C_v$. Let us define the scaled viscosity μ' by

$$\mu' = \frac{|\mathbf{M}|}{Re}\mu. \tag{2.11}$$

We introduce three nondimensional numbers hereafter, namely, the *Prandtl number Pr*, the *Mach number* \mathbf{M} and the *Reynolds number Re*

$$Pr = \frac{\mu C_p}{k}$$
, $\mathbf{M} = \frac{\mathbf{v}_0}{a_0}$, $Re = \frac{\rho |\mathbf{v}_0| L_r}{\hat{\mu}_0}$.

Then the nondimensional compressible N-S equations can be expressed in the same form of (2.1) and (2.2), namely,

$$\begin{cases}
\frac{\partial \rho}{\partial t} + \nabla \cdot (\rho \mathbf{v}) = 0, \\
\frac{\partial (\rho \mathbf{v})}{\partial t} + \nabla \cdot (\rho \mathbf{v} \otimes \mathbf{v} + p \mathbf{I}) = \nabla \cdot \boldsymbol{\tau}, \\
\frac{\partial (\rho E)}{\partial t} + \nabla \cdot (\rho \mathbf{v} H) = \nabla \cdot (\boldsymbol{\tau} \cdot \mathbf{v} - \mathbf{q}) + Q,
\end{cases} (2.12)$$

where the viscous stress is given by

$$\tau = \mu' \left[-\frac{2}{3} (\nabla \cdot \mathbf{v}) \mathbf{I} + \nabla \mathbf{v} + (\nabla \mathbf{v})^T \right], \tag{2.13}$$

and the nondimensional heat flux of the energy equation is written as

$$\mathbf{q} = -\frac{\mu'}{(\gamma - 1)Pr} \nabla T = -\frac{\gamma \mu'}{(\gamma - 1)Pr} \nabla \left(\frac{p}{\rho}\right). \tag{2.14}$$

And *Q* is a nondimensional volume heat source which is case-dependent.

In theory, the nondimensional compressible N-S equation can be recovered to the nondimensional F-S equation (2.8). For the F-S equation (2.8), applying the same nondimensionalization (2.9) leads to the following equation:

$$\frac{\partial \left[\frac{\rho T}{\gamma(\gamma-1)}\right]}{\partial t} = \frac{1}{\gamma(\gamma-1)} k_s \nabla^2 T + Q. \tag{2.15}$$

It can be verified that the energy evolution of the nondimensional compressible N-S equations (2.12) can degenerate to the same form (2.15) under the transformation relationship of Section 2.2.

Remark 2.1. According to (2.11), if $|\mathbf{M}| = \mathbf{0}$, the scaled viscosity μ' is zero and also independent of the Reynolds number Re. But if $|\mathbf{M}| \neq \mathbf{0}$, the recovery error from the N-S to the F-S equation can be large for a small Reynolds number. The time marching of the momentum equation could yield non-zero velocity solutions with non-zero shear stress, which eventually affect solver stability. In [18], solutions of small velocity are obtained so that the solutions only approximate the solid solutions of the F-S equation with certain recovery errors. A hard setting of null velocity leads to stability issues which are still unsolved in [18]. In our work, the velocity is allowed to be zero and the recovery to the F-S equation can be fully accomplished.

2.4 Initial condition

The solution vector of the compressible N-S equations in both the fluid and solid domains can be written in a unified form

$$\mathbf{U} = \begin{bmatrix} \rho \\ \rho \mathbf{v} \\ \rho E \end{bmatrix} = \begin{bmatrix} 1 \\ \mathbf{M} \\ \frac{1}{\gamma(\gamma - 1)} + \frac{1}{2} |\mathbf{M}|^2 \end{bmatrix}, \tag{2.16}$$

which can be solved by using regular time marching methods. For both the fluid and the solid, ρ and T are alway unit in the initial fields according to the nondimensionalization (2.9). With a zero Mach number, the initial solid field \mathbf{U}_0 is given by

$$\mathbf{U}_{0} = \begin{bmatrix} \rho \\ \rho \mathbf{v} \\ \rho E \end{bmatrix} = \begin{bmatrix} 1 \\ \mathbf{0} \\ \frac{1}{\gamma(\gamma - 1)} \end{bmatrix}. \tag{2.17}$$

Note that during the time-marching iteration, the conservative variables ρ and ρ **v** also participate in the computation of the solid field under the unified solution framework.

2.5 Boundary conditions

Five types of boundary conditions relative to solid heat transfer are included in the unified solution solver, which can be applied to both the fluid and the solid domains. They are isothermal, adiabatic, heat flux, heat convective, and surface radiation boundary conditions, in which the radiation boundary condition is provided for surface radiation computations. All the boundary conditions are imposed implicitly in the same way as the original N-S flow solver, see reference [12] for details. The boundary conditions are expressed in a nondimensional form as shown in Table 2, where the *Biot number* (Bi) is introduced for the convection boundary condition, namely, Bi = $\hat{h}L_r/k_0^s$; q_s is the normal heat flux and \hat{q}_e is the dimensional heat flux due to exterior heating up

such as solar radiation; T and T_{ref} are nondimensional, and the latter one denotes the reference temperature. Note that the nondimensional expressions must be computed correctly otherwise unphysical solutions might occur.

T 11 4	Ε.		_		12.2			10 .	
Table I.	FIVE.	tynes	Ωt	houndary	conditions	ın	the	nondimensiona	I torm
Tubic 1.	1110	Lypcs	O.	Dournaar y	Conditions		LIIC	Homannensiona	

B.C. Type	Nondimensional form				
Adiabatic	$q_s = 0$				
Isothermal	$T_{bc} = T_{ m w}$				
Heat flux	$q_s = \frac{1}{\gamma(\gamma - 1)} k_s \frac{\partial T}{\partial n}$				
Heat convective	$q_s = \frac{1}{\gamma(\gamma - 1)} \mathrm{Bi} \left(T - T_{\mathrm{ref}} \right)$				
Surface radiation	$q_s = \frac{\epsilon}{\gamma(\gamma - 1)} \frac{\sigma L_r}{k_0 T_0} \left[\left(\hat{T}^4 - \hat{T}_{\text{ref}}^4 \right) - \alpha \dot{\hat{q}}_e \right]$				

3 Numerical Methods

A parallel, high-order adaptive discontinuous Galerkin (DG) compressible N-S flow solver has been developed and tested for many benchmark problems in [9–14]. We keep the algorithms untouched so that all existing CFD methods implemented in this package can be utilized for solid heat conduction and conjugate fluid and solid heat transfer simulations. This section gives a brief overview of the basic spatial and temporal discretization schemes used in the solver. Without loss of generality, the proposed unified solution framework can be applied to other CFD solvers as well.

3.1 Modal discontinuous Galerkin method for spatial discretization

A modal discontinuous Galerkin method is used for spatial discretization in the solver [9,11]. The DG discretization of the N-S equations (2.1) is defined on a partition of the computational domain Ω of arbitrary shape and can handle curved elements. An adaptive discontinuous Galerkin method is applied, which seeks a variable-order approximation \mathbf{U} in each element $\mathcal{E} \in \Omega$ with a k-order polynomial, namely

$$\mathbf{U}(x,t) = \sum_{j=1}^{N(k)} \mathbf{u}_{j}(t)\psi_{j}(x), \tag{3.1}$$

where $\{\psi_j\}_{j=1}^{N(k)}$ is a basis for $P_k(\mathcal{E})$, the space of all polynomials defined on \mathcal{E} with order no more than k. An orthonormal basis set expressed in the Cartesian coordinates is used for supporting arbitrarily shaped elements [9, 11] and it also facilitates the implementation of adaptive computations [15]. The adaptive approximation can be

simply obtained by adding or removing terms of (3.1) in the orthonormal basis set with cell order *k* stored elementwisely.

Next, by multiplying Eq. (2.1) with the adaptive-order basis functions, a weak form is obtained as

$$\int_{\mathcal{E}} \psi_i \psi_j d\mathbf{x} \frac{d\mathbf{u}_j}{dt} = -\int_{\partial \mathcal{E}} \psi_i \widetilde{\mathbf{F}} \cdot \hat{\mathbf{n}} d\sigma + \int_{\mathcal{E}} (\mathbf{F} \cdot \nabla \psi_i + \psi_i \mathbf{S}) d\mathbf{x} := \mathbf{R}_i, \tag{3.2}$$

where Einstein's summation convention is used. Here \hat{n} denotes the outward unit normal of the surface element $\partial \mathcal{E}$. The flux terms containing the inviscid flux $\widetilde{\mathbf{F}}_c$ and the viscous flux $\widetilde{\mathbf{F}}_v$ are defined as

$$\widetilde{\mathbf{F}} = \widetilde{\mathbf{F}}_c \left(\mathbf{u}_h^{\pm} \right) + \widetilde{\mathbf{F}}_v \left(\mathbf{u}_h^{\pm}, (\nabla_h \mathbf{u}_h + \delta_f)^{\pm} \right), \tag{3.3}$$

where $\widetilde{\mathbf{F}}_c$ is computed by a Riemann solver with the two-side variables \boldsymbol{u}_h^\pm on the surface, and $\widetilde{\mathbf{F}}_v$ can be computed by several optional DG schemes [1,5,21]. In the current work, the second approach of Bassi and Rebay (BR2) [1] is used, which introduces the local and the global lifting operators δ_f and δ . The local lifting operator can be solved by using Galerkin projection from each element \mathcal{E} to the surface $\partial \mathcal{E}$

$$\int_{\mathcal{E}} \psi \cdot \delta_f \, \mathrm{d}x = \int_{\partial \mathcal{E}} \psi \cdot (\{u\} - u_h^+) \, \mathrm{d}\sigma, \tag{3.4}$$

where the average operator $\{a\} = \frac{1}{2}(a^+ + a^-)$ is used. In the BR2 scheme, the global lifting operator is used for volume integrations and the local lifting operator is used for facewise integrations. The global lifting operator is linked to the local lifting operator in the following way

$$\delta = \sum_{\partial \mathcal{E}} \delta_f. \tag{3.5}$$

The volume integration terms of (3.2) containing the global lift operator can be computed as

$$\mathbf{F} = \mathbf{F}_{c}(u_{h}) + \mathbf{F}_{v}(u_{h}, (\nabla_{h}u_{h} + \delta)). \tag{3.6}$$

The implementation of exponential integrator-based time integration schemes for the BR2 formulation uses the same analytical global Jacobian as in [12, 13], which is composed of variable-order elemental Jacobians for both the fluid and solid domains.

3.2 Exponential time integrator

Exponential integrators [2, 3, 7] have widely been studied as effective tools for the time marching of various evolution problems in science and engineering in the past decades. The Predictor-Corrector EXPonential time integrator scheme (PCEXP) was proposed in [11] for fast time integration of the unified system of the fluid and the solid domains. The PCEXP scheme allows large time steps and is found to be efficient for both steady and unsteady flow computations [10, 12–14].

Let us start with the following ordinary differential system

$$\frac{\mathrm{d}\mathbf{u}}{\mathrm{d}t} = \mathbf{R}(\mathbf{u}),\tag{3.7}$$

where $\mathbf{u} = \mathbf{u}(t) \in \mathbb{R}^K$ denotes the solution vector, $\mathbf{R}(\mathbf{u}) \in \mathbb{R}^K$ is the right-hand-side term obtained by the DG discretization, and K is the total degree of freedom of the solution. Let us consider $\mathbf{u}(t)$ in the interval of one time step, *i.e.*, $t \in [t_n, t_{n+1}]$. Rewriting the right-hand-side term of (3.7) leads to

$$\frac{\mathrm{d}\mathbf{u}}{\mathrm{d}t} = \mathbf{J}_n \mathbf{u} + \mathbf{N}(\mathbf{u}),\tag{3.8}$$

with the Jacobian matrix

$$\mathbf{J}_n = \frac{\partial \mathbf{R}(\mathbf{u}_n)}{\partial \mathbf{u}},$$

and the remainder part

$$N(u) = R(u) - J_n u.$$

Thus, Eq. (3.8) admits the following solution

$$\mathbf{u}_{n+1} = \exp(\Delta t \, \mathbf{J}_n) \mathbf{u}_n + \int_0^{\Delta t} \exp\left((\Delta t - \tau) \, \mathbf{J}_n\right) \mathbf{N}(\mathbf{u}(t_n + \tau)) \, d\tau, \tag{3.9}$$

where the matrix exponential is defined as

$$\exp(-t\mathbf{J}_n) = \sum_{m=0}^{\infty} \frac{\left(-t\mathbf{J}_n\right)^m}{m!}$$
(3.10)

The PCEXP scheme [12] that approximates (3.9) is given by

$$\mathbf{u}^* = \mathbf{u}_n + \Delta t \, \mathbf{\Phi}_1(\Delta t \mathbf{J}_n) \mathbf{R}(\mathbf{u}_n), \tag{3.11}$$

$$\mathbf{u}_{n+1} = \mathbf{u}^* + \frac{1}{2} \Delta t \, \mathbf{\Phi}_1(\Delta t \mathbf{J}_n) \left[(\mathbf{N}(\mathbf{u}^*) - \mathbf{N}(\mathbf{u}_n)) \right], \tag{3.12}$$

with the matrix function Φ_1 defined as

$$\mathbf{\Phi}_{1}(\Delta t \mathbf{J}_{n}) := \frac{\mathbf{J}_{n}^{-1}}{\Delta t} \left[\exp \left(\Delta t \mathbf{J}_{n} \right) - \mathbf{I} \right], \tag{3.13}$$

where I is a $K \times K$ identity matrix. The PCEXP scheme behaves like an implicit scheme and is efficient for simulating both steady and unsteady flows [10–12]. The time advancement procedure using PCEXP in the solid domain is identical to that of the original CFD solver. For solid heat transfer, the time step size is often controlled by the Fourier number Fo, namely,

$$\Delta t = Fo \frac{h^2}{\alpha (p+1)^2},\tag{3.14}$$

where h denotes the spatial mesh size, α the thermal diffusivity, and p the spatial order of accuracy. To use large time steps for the PCEXP scheme, a dynamically increasing Fourier number law is taken which is similar to the CFL number evaluation strategy presented in [11]. The resulting solid solver is found to be stable for very large time steps with a Fourier number up to 10^8 , as shown in Section 4.4.

4 Numerical Results

In this section, we first compare numerical results obtained by solving the three-dimensional compressible N-S equations with corresponding analytical solutions of the one-dimensional F-B equation and verify their accuracy in Cases 4.1 - 4.3, where the spatial order k or DG (P_k) is chosen to be equal to the order of the exact polynomial solutions. For Case 4.4, the exact solution is non-polynomial and the convergence orders are computed to verify the high-order numerical feature for solving solid problems. Finally, a three-dimensional heat sink problem is presented in Case 4.5 for demonstrating the feasibility of using the adaptive high-order unified solution solver for solid heat conduction applications.

4.1 Verification of heat flux boundary condition

The heat flux boundary condition is tested with a steady one-dimensional solid heat conduction problem with constant thermal conductivity $k_s = 400 \text{ W/m} \cdot \text{K}$ and no heat generation in the medium. We take the left wall to be at temperature $T_w = 300 \text{ K}$ at x = 0 and the heat flux boundary condition with heat flux of $q = 20 \text{W/cm}^2$ at x = L = 0.028 m is applied. The analytical solution of this problem is governed by the following simplified heat conduction equation

$$\frac{\mathrm{d}^2 T}{\mathrm{d}x^2} = 0. \tag{4.1}$$

and the analytical solution is given by

$$T(x) = -Ax + T_{w}, (4.2)$$

where $A = q/k_s$. We compute a numerical solution with the 3-D compressible N-S equations discretized by DG (P_1) on a single cell. As one can see from Fig. 1, the numerical solution approximates the exact solution in high precision in the computational domain with errors floating around 10^{-14} .

4.2 Verification of convection boundary condition

The convection boundary condition is often essential for simulating conjugate heat transfer problems. To test the unified solution solver along with the convection boundary condition, the following one-dimensional solid heat conduction problem (4.3) with

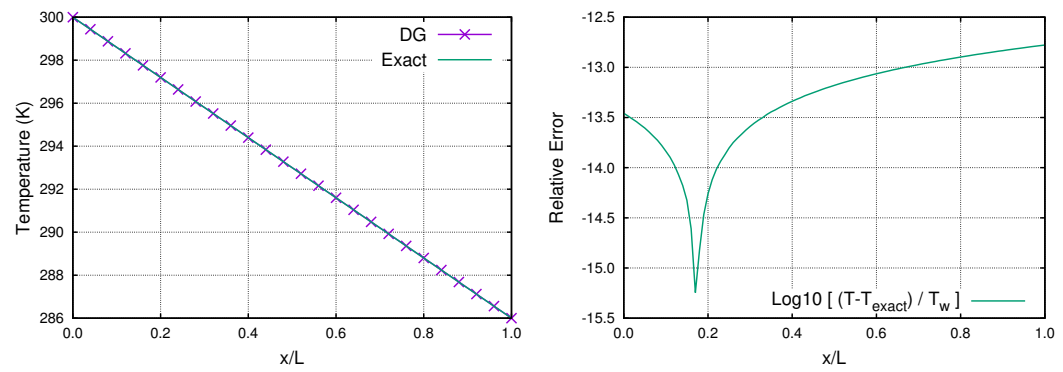


Figure 1: The numerical solution (left) and its relative errors (right) in Case 4.1.

volume heat source $Q = 5 \times 10^5 \,\text{W/m}^3$ is considered:

$$k\frac{d^2T}{dx^2} + Q = 0. (4.3)$$

Here we take the left wall to be at temperature $T_{\rm w}=300~{\rm K}$ at x=0 and the convection boundary condition $-k_s\frac{\partial T}{\partial x}=h\left(T-T_0\right)$ is applied at $x=L=1~{\rm m}$. The thermal conductivity $k_s=400~{\rm W/m\cdot K}$, the heat transfer coefficient $h=600~{\rm W/m^2\cdot K}$ and $T_0=273.15~{\rm K}$. The analytical solution of this problem is given by

$$T(x) = -\frac{1}{2}Ax^2 + \left(\frac{T_0 - T_w}{1+s} + \frac{2s+1}{s+1}A\right)x + T_w,\tag{4.4}$$

where $A = Q/k_s$ and $s = k_s/h$. We compute the solution with DG (P_2) for matching the exact quadratic solution (4.4). Again, the simulated solution approximates the exact solution with high accuracy as shown in Fig. 2, and the relative errors are almost invisible in the global and the local error floats.

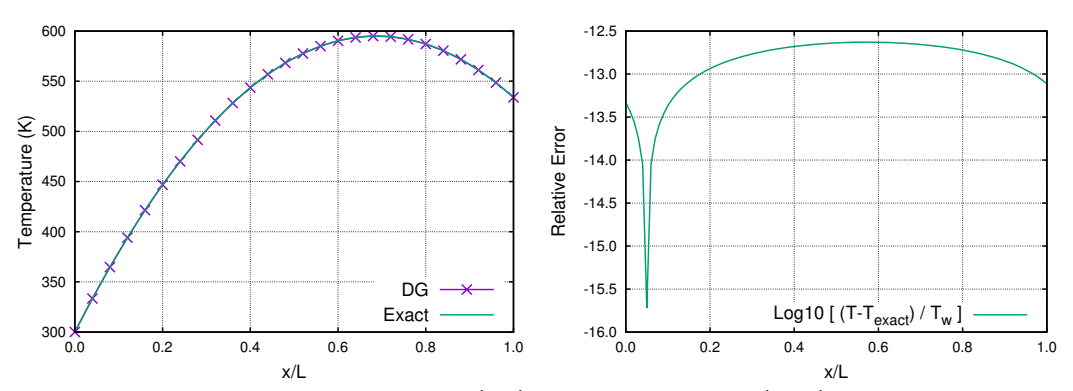


Figure 2: The numerical solution (left) and its relative errors (right) in Case 4.2.

4.3 Verification of radiation boundary condition

Apart from the usual boundary conditions considered above, the radiation boundary condition is also provided in the unified solver. The radiation boundary condition is tested with a solar heating wall problem. Consider a large plane wall of thickness L=0.06 m and thermal conductivity $k_s=1.2$ W/m·K. The wall is covered with white porcelain tiles that have an emissivity of $\epsilon=0.85$ and a solar absorptivity of $\alpha=0.26$. The Stefan-Boltzmann constant $\sigma=5.670374419\times 10^{-8}$ W·m·K⁻⁴. The inner wall surface has a temperature of $T_1=300$ K while the outer surface is exposed to solar radiation that is incident at a rate of $\dot{q}_e=800$ W/m². The reference temperature of radiation is at $T_r=0$ K. This benchmark problem is governed by a steady heat conduction equation

$$\frac{\mathrm{d}^2 T}{\mathrm{d}x^2} = 0,\tag{4.5}$$

with isothermal and radiation boundary conditions

$$T(0) = T_1,$$
 $-k_s rac{\mathrm{d}T(L)}{\mathrm{d}r} = \epsilon \sigma \left[T^4(L) - T_r^4 \right] - \alpha \dot{q}_e.$

The analytical solution of this problem can be expressed as

$$T(x) = \frac{1}{k_s} \left(\alpha \dot{q}_e - \epsilon \sigma T_L^4 \right) x + T_1, \tag{4.6}$$

which is the solution for the variation of the temperature in the wall in terms of the unknown outer surface temperature T_L . At x = L, the equation (4.6) becomes

$$T_L = \frac{L}{k_s} \left(\alpha \dot{q}_e - \epsilon \sigma T_L^4 \right) + T_1. \tag{4.7}$$

Finally, the temperature solution (4.6) can be closed with T_L numerically solved from the nonlinear equation (4.7). The numerical solution is computed with DG (P_1). One more time, although one cell is used for the computational domain, the numerical solution agrees very well with the exact solution, as shown in Fig. 3 (left). The local errors float around 10^{-14} along the computational domain as demonstrated in Fig. 3 (right).

4.4 Heat conduction of a hollow cylinder

In this case, the convergence order of accuracy of the developed unified solver is tested on a 3-D solid hollow cylinder problem. The isothermal boundary condition is imposed on the inner and the outer cylinder surfaces with $T_i = 1$ and $T_0 = 5$ at radius of $r_i = 1$ and $r_0 = 2$, respectively. The 3-D hollow cylinder is obtained by extruding the 2-D annular surface of the *xy*-plane with $\Delta z = 1$. The periodic boundary condition is

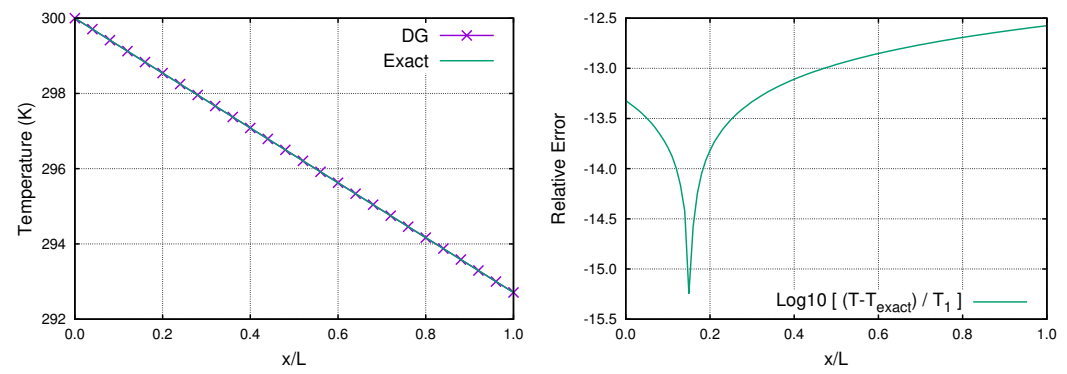


Figure 3: The numerical solution (left) and its relative errors (right) in Case 4.3.

imposed on the two annular surfaces. Quadratic curved elements are used for representing boundary curvatures of the inner and the outer cylinder surfaces. The exact solution of this problem is given by

$$T_{\text{exact}}(r) = T_o + (T_i - T_o) \frac{\ln r - \ln r_o}{\ln \frac{r_i}{r_o}},$$
 (4.8)

where r denotes the horizontal radius. This exact solution is used to study the convergence rate of numerical solutions by measuring the L_2 norms of the numerical temperature errors over the entire computational domain Ω . The scaled L_2 error is defined as

$$E_{L_2} = \sqrt{\frac{\int \left[T_{\rm NS} - T_{\rm exact}\right]^2 d\Omega}{\int d\Omega}}$$
 (4.9)

Three successively refined meshes $[nb \times nr \times nz] = [16 \times 4 \times 1,32 \times 8 \times 1,64 \times 16 \times 1]$ are generated for calculating the convergence order, where nb, nr, nz denotes the cell number along the annular boundaries, the radical direction and the z direction, respectively. We compute the temperature solution of the N-S equations $T_{\rm NS}$ with DG (P_4) . As shown in Table 2, $T_{\rm NS}$ converges to the exact solution rapidly with mesh refinements. The average convergence order is 4.5, which verifies the ability of the proposed solver for obtaining high-order solid solutions.

Table 2: Numerical errors for the simulated heat conduction of a hollow cylinder in Case 4.4: convergence order in space with the DG P_4 discretization.

$nb \times nr \times nz$	$16 \times 4 \times 1$	$32 \times 8 \times 1$	$64 \times 16 \times 1$	avg. order
E_{L_2}	6.4067×10^{-5}	2.9389×10^{-6}	1.2803×10^{-7}	4.50

4.5 Heat sink problem

In this case, we will test the ability of using the advanced high-order adaptive method existing in the original N-S flow solver for solid heat conduction applications. A 3-D heat sink problem is considered which models a CPU heat sink. The geometry contains thirteen solid fins, where the bottom size is of $100 \text{mm} \times 100 \text{mm} \times 5 \text{mm}$ and the fin size is of $1 \text{mm} \times 100 \text{mm} \times 50 \text{mm}$. The bottom surface has a constant temperature of $T = 100^{\circ}\text{C}$. Other surfaces are modeled with the convection boundary condition with the thermal conductivity $k = 400 \text{ W/m} \cdot \text{K}$, the heat transfer coefficient $h = 1000 \text{ W/m}^2 \cdot \text{K}$ and the reference temperature $T_0 = 30^{\circ}\text{C}$.

The computational mesh for this model contains 115,000 unstructured, anisotropic hexahedral elements with a cell aspect ratio of 10, see Fig. 5(a) for illustration. The numerical results are produced by using the proposed unified DG solver, in particular, the adaptive DG (P_{0-k}) approach [14, 15] is used in which the solution is initially computed with the P_0 order and then converted to the P_k order adaptively in space. In total, five different accuracy solutions can be obtained as the polynomial order k increases from zero to four during a single zigzag alike convergence, as shown in Fig. 4(a). To demonstrate the ability of using large time steps, adaptive time stepping with a variable Fourier number *Fo* is used during the spatial adaptation. The Fourier number starts at 10^2 and dynamically increases up to 10^8 (see Fig. 4(b)). Thus, the resultant unified solver is capable of solving the solid problems with both adaptive spatial accuracy and variable time steps. The converged, adaptive polynomial order distribution (P) for DG discretization is presented In Fig. $5(b)_{r}$, and it can be observed that the P₄ elements are located in the lower part of the fins where the strong nonlinear distribution appears. The P_3 and P_2 elements are distributed in the medium gradient varying zones along the anisotropic direction aligned with the fins. The computed temperature data is extracted along the median intersection curve cut by the red plane as shown in Fig. 6(a). Fig. 6(b) gives the temperature profiles obtained on the closed intersection curve containing both upper, lower, and side surfaces, and five solutions with respect to different maximal orders $k(P_{0-k})$ are also displayed in different colors. It can be observed that the temperature distribution is visibly influenced by the order of approximation accuracy, and the P_{0-4} adaptive solution (green line) can catch and exhibit significant temperature variations. In this case, the adaptive solution robustly converges to the steady-state solution and the final order distribution over the total number of elements are $P_1 - 0.49\%$, $P_2 - 67.58\%$, $P_3 - 27.15\%$, and $P_4 - 4.78\%$.

5 Conclusions

We propose to develop a unified solution framework for simulating conjugate fluid and solid heat transfer, in which the solution is solely governed by the compressible N-S equations. This paper serves as Part I of this framework, in which we focus on capability verification of the unified solver for solid heat conduction problems. The theoretical connection between the fluid and solid domains is explained based on the

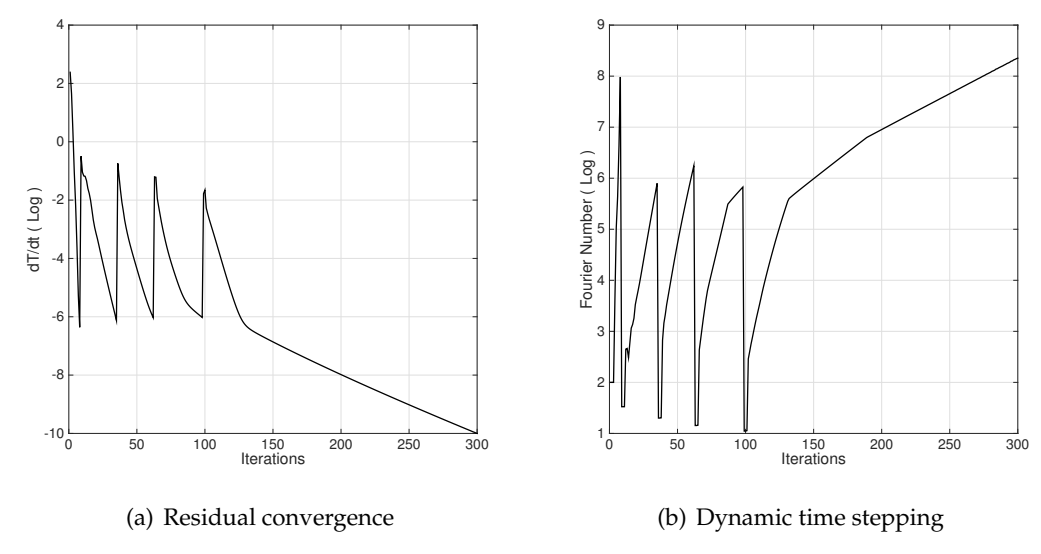


Figure 4: The heat sink simulated by the adaptive DG solid heat conduction solver in Case 4.5: (a) the convergence history of residuals; (b) Fourier number v.s the number of time iterations.

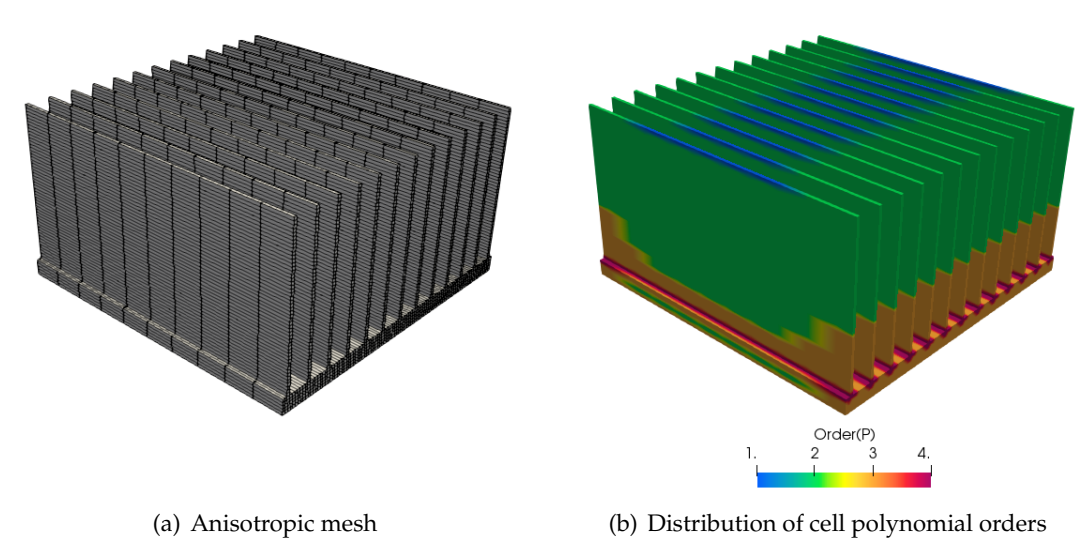
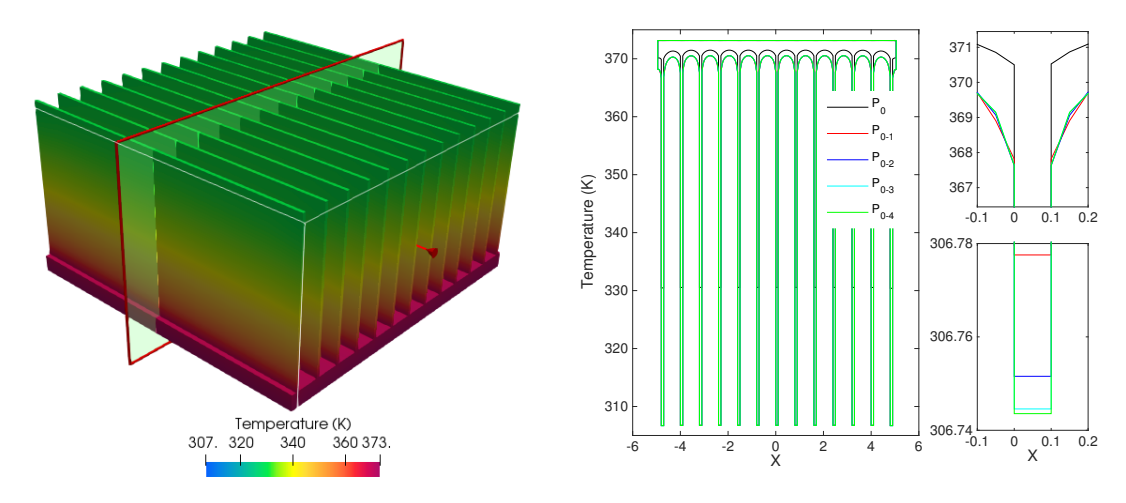


Figure 5: The heat sink simulated with the adaptive DG solid heat conduction solver in Case 4.5: (a) the anisotropic mesh generated with the cell aspect ratio of 10; (b) the perspective view of the distribution of cell polynomial orders. The solution is locally adapted from P_0 to P_4 , and the solver produces no P_0 cells in the end, indicating that the first-order spatial accuracy is inadequate for this problem.

compressible N-S equations in a nondimensionalized form. It is shown that the F-B equation is a specific form of the energy equation of the N-S equations with solid material parameters. The initial and boundary conditions are also discussed for both the fluid and the solid domains. Various test cases demonstrate that the proposed unified solution method is capable of simulating solid heat conduction by using an



- (a) Simulated temperature disctribution
- (b) Temperature profile along the cut plane

Figure 6: The heat sink solution produced by the adaptive DG solid heat conduction solver in Case 4.5. (a) the simulated temperature distribution and the cut plane; (b) the temperature profile along the cut plane and local cell polynomial orders.

high-order adaptive DG solver and an exponential time integrator for the N-S equations. The unified solver for solving conjugate fluid and solid heat transfer problems will be presented as Part II of this framework in the coming work, and the proposed method is applicable to other existing advanced N-S flow solvers as well.

Acknowledgments

S.-J. Li acknowledges the support from the National Natural Science Foundation of China (NSFC) under grant U1930402. L. Ju's work is partially supported by U.S. National Science Foundation DMS-2109633.

References

- [1] F. Bassi, S. Rebay, A high-order accurate discontinuous finite element method for the numerical solution of the compressible Navier-Stokes equations, Journal of Computational Physics, 131 (1997), 267–279.
- [2] S. M. Cox, P. C. Matthews, Exponential time differencing for stiff systems, Journal of Computational Physics, 176 (2002), pp. 430–455.
- [3] Q. Du, L. Ju, X. Li, Z. H. Qiao, Maximum bound principles for a class of semilinear parabolic equations and exponential time differencing schemes, SIAM Review, 63 (2021), pp. 317–359.
- [4] M. B. Giles, Stability analysis of numerical interface conditions in fluid-structure thermal analysis, International Journal for Numerical Methods in Fluids, 25 (1997), 421–436.

- [5] F. Gao, X. Ye, S. Zhang, A Discontinuous Galerkin Finite Element Method without Interior Penalty Terms, Advances in Applied Mathematics and Mechanics, 14 (2022), 299–314.
- [6] W. D. Henshaw, K. K. Chand, A composite grid solver for conjugate heat transfer in fluid-structure systems, Journal of Computational Physics, 228 (2019), 206–225.
- [7] M. Hochbruck, A. Ostermann, Exponential integrators, Acta Numerica, 19 (2010), pp. 209–286.
- [8] V. Kazemi-Kamyab, A. H. Van Zuijlen, H. Bijl, Analysis and application of high order implicit Runge–Kutta schemes for unsteady conjugate heat transfer: A strongly-coupled approach, Journal of Computational Physics, 272 (2014), 471–486.
- [9] S.-J. Li, A parallel discontinuous Galerkin method with physical orthogonal basis on curved elements, Procedia Engineering, 61 (2013), 144–151.
- [10] S.-J. Li, Z. J. Wang, L. Ju, L.-S. Lu, Explicit large time stepping with a second-order exponential time integrator scheme for unsteady and steady flows, AIAA paper, #0753, 2017.
- [11] S.-J. Li, L.-S. Luo, Z. J. Wang, L. Ju, An exponential time-integrator scheme for steady and unsteady inviscid flows, Journal of Computational Physics, 365 (2018), 206–225.
- [12] S.-J. Li, Z. J. Wang, L. Ju, L.-S. Lu, Fast time integration of Navier-Stokes equations with an exponential-integrator scheme, AIAA paper, #0369, 2018.
- [13] S.-J. Li, L. Ju, Exponential time-marching method for the unsteady Navier-Stokes equations, AIAA paper, #0907, 2019.
- [14] S.-J. Li, L. Ju, H. Si, Adaptive exponential time integration of the Navier-Stokes equations. AIAA paper, #2033, 2020.
- [15] S.-J. Li, Time advancement of the Navier-Stokes equations: p-adaptive exponential methods. Journal of Flow Control, Measurement & Visualization, 8 (2020), 63–76.
- [16] S.-J. Li, Efficient steady flow computations with exponential multigrid methods. In: Garanzha V.A., Kamenski L., Si H. (eds) Numerical Geometry, Grid Generation and Scientific Computing. Lecture Notes in Computational Science and Engineering, 143 (2021), 375–390, Springer.
- [17] L. Mangani, M. Darwish, L. Hanimann, A. Al Abed, E. Casartelli, F. Moukalled, A fully implicit conjugate heat transfer method, Numerical Heat Transfer, Part B: Fundamentals, 78 (2020), 175–196.
- [18] J. Nordström, B. Jens, Conjugate heat transfer for the unsteady compressible Navier-Stokes equations using a multi-block coupling. Computer &Fluid, 72 (2013), 20–29.
- [19] D. Reinert, A. Dwivedi, G. V. Candler, Verification of a conjugate heat transfer tool with US3D. AIAA paper, #1892, 2019.
- [20] S. Scholl, B. Janssens, T. Verstraete, Stability of static conjugate heat transfer coupling approaches using Robin interface conditions, Computers & Fluids, 172 (2018), 209–225.
- [21] Z. Sun, J. Liu, P. Wang, A discontinuous Galerkin method by patch reconstruction for convection-diffusion problems, Advances in Applied Mathematics and Mechanics, 12 (2020), 729–747.
- [22] A. Veeraragavan, J. Beri, R. J. Gollan, Use of the method of manufactured solutions for the verification of conjugate heat transfer solvers, Journal of Computational Physics, 307 (2016), 308–320.
- [23] N. Wansophark, A. Malatip, and P. Dechaumphai, Streamline upwind finite element method for conjugate heat transfer problems. Acta Mech Sinica, 21 (2005), 436–443.
- [24] G. Xie, B. Sundén, Comparisons of heat transfer enhancement of an internal blade tip with metal or insulating pins, Advances in Applied Mathematics and Mechanics, 3 (2011), 297–309.

[25] S. Zhang, F. Chen, H. Liu, Time-adaptive, loosely coupled strategy for conjugate heat transfer problems in hypersonic flows, Journal of Thermophysics and Heat Transfer, 28 (2014), 635–646.

[26] J. Zhao, S. Liu, T. Liu, A modified kernel method for solving Cauchy problem of twodimensional heat conduction equation. Advances in Applied Mathematics and Mechanics, 7 (2015), 31–42.